

Phase structure of two-color QCD at real and imaginary chemical potentials; lattice simulations and model analyses

Takahiro Makiyama,^{1,*} Yuji Sakai,^{2,†} Takuya Saito,^{3,‡} Masahiro Ishii,^{4,§} Junichi Takahashi,^{4,¶} Kouji Kashiwa,^{5,**} Hiroaki Kouno,^{1,††} Atsushi Nakamura,^{6,‡‡} and Masanobu Yahiro^{4,§§}

¹*Department of Physics, Saga University, Saga 840-8502, Japan*

²*Riken, Saitama 351-0198, Japan*

³*Integrated Information Center, Kochi University, Kochi 780-8520, Japan*

⁴*Department of Physics, Graduate School of Sciences, Kyushu University, Fukuoka 812-8581, Japan*

⁵*Yukawa Institute for Theoretical Physics, Kyoto University, Kyoto 606-8502, Japan*

⁶*Research Institute for Information Science and Education, Hiroshima University, Higashi-Hiroshima 739-8527, Japan*

(Dated: June 15, 2021)

We investigate the phase structure of two-color QCD at both real and imaginary chemical potentials (μ), performing lattice simulations and analyzing the data with the Polyakov-loop extended Nambu–Jona-Lasinio (PNJL) model. Lattice QCD simulations are done on an $8^3 \times 4$ lattice with the clover-improved two-flavor Wilson fermion action and the renormalization-group improved Iwasaki gauge action. We test the analytic continuation of physical quantities from imaginary μ to real μ by comparing lattice QCD results calculated at real μ with the result of analytic function the coefficients of which are determined from lattice QCD results at imaginary μ . We also test the validity of the PNJL model by comparing model results with lattice QCD ones. The PNJL model is good in the deconfinement region, but less accurate in the transition and confinement regions. This problem is improved by introducing the baryon degree of freedom to the model. It is also found that the vector-type four-quark interaction is necessary to explain lattice data on the quark number density.

PACS numbers: 11.15.Ha, 12.38.Gc, 12.38.Mh, 25.75.Nq

I. INTRODUCTION

Exploration of QCD phase diagram is one of the most important subjects in not only nuclear and particle physics but also cosmology and astrophysics. However, due to the complexity of fermion determinant, the first principle calculation, i.e., lattice QCD (LQCD) simulations are quite difficult at high quark number chemical potential μ . The QCD partition function Z at finite temperature T and finite μ is expressed by

$$Z = \int DU \det[M(\mu)] e^{-S_G}, \quad (1)$$

where U_μ ($\mu = 1, 2, 3, 4$) and S_G are the link variables and the pure gauge action, respectively, and $M(\mu)$ is written as

$$M(\mu) = \gamma_\mu D_\mu + m - \mu \gamma_4 \quad (2)$$

with the covariant derivative D_μ and the quark mass m in the continuum limit. For later convenience, we regard μ as a complex variable. It is easy to verify

$$\{\det[M(\mu)]\}^* = \det[M(-\mu^*)]. \quad (3)$$

Hence, the fermion determinant $\det[M(\mu)]$ is not real when μ is real, and the importance sampling technique does not work in the Monte Carlo simulations there. This is the well-known sign problem. Several methods were proposed so far to resolve this problem; these are the reweighting method [1], the Taylor expansion method [2, 3], the analytic continuation from imaginary μ to real μ [4–10], the complex Langevin method [11–13] and the Lefschetz thimble theory [14, 15]. However, these are still far from perfection.

On the contrary, in two color QCD (QC₂D), the lattice simulations can be made at real and finite μ , since the theory has no sign problem [16–19]. In fact, the following relation is obtained:

$$\begin{aligned} \det[M(\mu)] &= \det[(t_2 C \gamma_5)^{-1} M(\mu) (t_2 C \gamma_5)] \\ &= (\det[M(\mu^*)])^*, \end{aligned} \quad (4)$$

where t_2 and $C = \gamma_2 \gamma_4$ are the second Pauli matrix in color space and the charge conjugation matrix, respectively. Obviously, $\det[M(\mu)]$ is real when μ is real. Recently, Hands et al. analyzed the phase structure of QC₂D in a wide range of real μ by using two-flavor Wilson fermions [20, 21]. QC₂D can be also used to check the validity of methods proposed to resolve the sign problem. In fact, Cea et al. [22, 23] tested the validity of analytic continuation from imaginary μ to real μ with staggered fermions.

Equation (3) shows that $\det[M(\mu)]$ is real when μ is pure imaginary, i.e., $\mu = i\mu_I = i\theta T$ for real variables μ_I and θ , so that LQCD simulations are feasible there. Observables at real μ are extracted from those at imaginary μ with analytic continuation. In the analytic continuation, we must pay attention to the structure of phase diagram in the imaginary μ region

*12634019@edu.cc.saga-u.ac.jp

†ysakai@riken.jp

‡tsaitou@kochi-u.ac.jp

§ishii@email.phys.kyushu-u.ac.jp

¶takahashi@phys.kyushu-u.ac.jp

**kouji.kashiwa@yukawa.kyoto-u.ac.jp

††kounoh@cc.saga-u.ac.jp

‡‡nakamura@riise.hiroshima-u.ac.jp

§§yahiro@phys.kyushu-u.ac.jp

where QCD has two characteristic properties, the Roberge-Weiss (RW) periodicity and the RW transition [24]. The QCD grand partition function has a periodicity of $2\pi/N_c$ in θ :

$$Z(\theta) = Z\left(\theta + \frac{2\pi k}{N_c}\right) \quad (5)$$

for integer k and the number of color N_c . This periodicity was found by Roberge and Weiss and is then called the RW periodicity. Roberge and Weiss also showed that a first-order phase transition occurs at $T \geq T_{\text{RW}}$ and $\theta = (2k+1)\pi/N_c$. This transition is named the RW transition, and T_{RW} is slightly larger than the pseudo-critical temperature T_{c0} of deconfinement transition at zero μ . These features are remnants of Z_{N_c} symmetry in the pure gauge limit. These properties are confirmed by LQCD simulations [4–10, 22, 23].

The RW periodicity does not mean that Z_{N_c} symmetry is exact. Hence, there is no a priori reason that the order parameter for Z_{N_c} symmetry such as the Polyakov loop Φ is zero in the confinement phase. In fact, in the case of $N_c = 3$, the Polyakov loop is always finite even in the confinement phase, when T is finite. However, the case of $N_c = 2$ is special [22]. In this case, the action and the boundary conditions are invariant at $\mu_1/T = (2k+1)\pi/2$ under the $\mathcal{C}Z_2$ transformation composed of the Z_2 transformation and charge conjugation \mathcal{C} [25]. Due to this symmetry, the Polyakov loop becomes zero at low T when $\mu_1/T = (2k+1)\pi/2$. Paying attention to these characteristic features, Cea et al. [22, 23] analyzed the validity of analytic continuation in QC₂D and found that lattice QC₂D (LQC₂D) data at real μ can be described by a suitable analytic function, when the coefficients of analytic function are determined from LQC₂D data at imaginary μ .

The results of LQCD at imaginary μ are also useful to determine the parameters of effective models, such as the Polyakov-loop extended Nambu–Jona-Lasinio (PNJL) model [26–32]. Here we call this approach “imaginary chemical potential matching approach” [33]. It is known that the PNJL model can reproduce the results of LQCD at imaginary μ , at least qualitatively, since the model has the RW periodicity and the RW transition [34, 35]. It was proposed [36] that the strength G_v of vector-type four-quark interaction [37, 38], which is expected to be important for the physics of neutron stars, may be determined from LQCD data at imaginary μ ; for the relation between neutron star properties and G_v , see Ref. [39] and references therein. In Refs. [40] and [41], in fact, G_v is determined with this prescription. The validity of such a determination of parameters in effective models can be checked in QC₂D.

In this paper, we study the phase structure of QC₂D at both real and imaginary μ by performing simulations on an $8^3 \times 4$ lattice with the renormalization-group improved Iwasaki gauge action [42, 43] and the clover-improved two-flavor Wilson fermion action [44] and analyzing the QC₂D data with the PNJL model. We first test the analytic continuation from imaginary μ to real μ by comparing LQC₂D data calculated at real μ with the result of analytic function the coefficients of which are determined from LQC₂D data at imaginary μ . Such a test was tested in Refs. [22, 23] with staggered fermions. Here the test is made with clover-improved Wilson

fermions by assuming a polynomial series in the deconfinement phase and a Fourier series in the confinement phase.

We second test the validity of the PNJL model by comparing LQC₂D results with model ones. The PNJL model is good in the deconfinement region, but less accurate in the confinement region. This problem is improved by introducing the baryon degree of freedom to the model. It is also found that the vector-type four-quark interaction is necessary to explain QC₂D data on the quark number density n_q .

This paper is organized as follows. Section II presents the lattice action and the parameter setting used in our LQC₂D simulations. The definition of physical quantities is also presented. In Sec. III, the PNJL model is recapitulated. In Sec. IV, numerical results of LQC₂D are shown and the analytical continuation of physical quantity from imaginary μ to real μ is tested. Comparison between LQC₂D data and PNJL results are made in Sec. V. Section VI is devoted to a summary.

II. LATTICE SIMULATIONS

A. Lattice action

We use the renormalization-group-improved Iwasaki gauge action S_G [42, 43] and the clover-improved two-flavor Wilson quark action S_Q [44] defined by

$$S = S_G + S_Q, \quad (6)$$

$$S_G = -\beta \sum_x \left(c_0 \sum_{\mu < \nu; \mu, \nu=1}^4 W_{\mu\nu}^{1 \times 1}(x) + c_1 \sum_{\mu \neq \nu; \mu, \nu=1}^4 W_{\mu\nu}^{1 \times 2}(x) \right), \quad (7)$$

$$S_Q = \sum_{f=u,d} \sum_{x,y} \bar{q}_x^f M_{x,y} q_y^f, \quad (8)$$

where q is the quark field, $\beta = 4/g^2$, $c_1 = -0.331$, $c_0 = 1 - 8c_1$, and

$$M_{x,y} = \delta_{xy} - \kappa \sum_{i=1}^3 \{ (1 - \gamma_i) U_{x,i} \delta_{x+\hat{i},y} + (1 + \gamma_i) U_{y,i}^\dagger \delta_{x,y+\hat{i}} \} - \kappa \{ e^\mu (1 - \gamma_4) U_{x,4} \delta_{x+\hat{4},y} + e^{-\mu} (1 + \gamma_4) U_{y,4}^\dagger \delta_{x,y+\hat{4}} \} - \delta_{xy} c_{\text{sw}} \kappa \sum_{\mu < \nu} \sigma_{\mu\nu} F_{\mu\nu}. \quad (9)$$

Here κ is the hopping parameter, $F_{\mu\nu}$ is the lattice field strength and $F_{\mu\nu} = (f_{\mu\nu} - f_{\mu\nu}^\dagger)/(8i)$ with $f_{\mu\nu}$ the standard clover-shaped combination of gauge links.

The coefficient c_{sw} of clover term is determined by using a result obtained in a perturbative mean-field improved value $c_{\text{sw}} = P^{-3/4}$ [45] with the plaquette P calculated in one-loop perturbation theory, $P = 1 - 0.3154\beta^{-1}$ for $N_c = 2$ [46].

B. Parameter setting for simulations

We denote temporal and spatial lattice sizes as N_t and N_s , respectively. The Hybrid Monte-Carlo algorithm is used to generate full QC₂D configurations with two-flavor dynamical quarks. The simulations are performed on a lattice of $N_s^3 \times N_t = 8^3 \times 4$. The step size of molecular dynamics is $\delta\tau = 0.02$ and the step number of the dynamics is $N_\tau = 50$. The acceptance ratio is more than 95%. We generated 10,000 trajectories and removed the first 5,000 trajectories as thermalization for all the parameter set. The relation of parameters κ and β to the corresponding T/T_{c0} is determined by finding the line of constant physics where the ratio of the pseudo-scalar (PS) meson mass m_{ps} to the vector meson mass m_v at $T = \mu = 0$ are invariant; see Table I for the relation.

N_s	N_t	β	κ	T/T_{c0}
8	4	0.60000	0.13782	0.87783(585)
		0.64000	0.13770	0.94126(628)
		0.66000	0.13751	0.98577(657)
		0.68000	0.13695	1.02608(84)
		0.70000	0.13677	1.06282(709)
		0.72000	0.13679	1.11629(745)
		0.74000	0.13567	1.16526(77)
		0.76000	0.13493	1.20197(802)
		0.78000	0.13443	1.24298(829)

TABLE I: Summary of simulation parameters. T_{c0} is the pseudo-critical temperature at $\mu = 0$. In this parameter setting, the lattice spacing a is about $1.38 \sim 1.96 \text{ GeV}^{-1}$ and the ratio m_{ps}/m_v is 0.8 at $T = 0$.

C. Physical observables

In this paper, we calculate the Polyakov loop (Φ), the quark number density (n_q) and the chiral condensate (σ). The quark number density is calculated by

$$n_q = \frac{T}{V} \frac{\partial}{\partial \mu} \log Z, \quad (10)$$

where V is the spatial volume, and σ is by

$$\sigma = \langle \bar{q}q \rangle, \quad (11)$$

where q is quark field and the $\langle O \rangle$ is the average value of physical quantity O . The chiral condensate suffers from the renormalization, and chiral symmetry is explicitly broken by Wilson fermions. This makes it difficult to deal with the absolute value of chiral condensate itself. We then consider a variation

$$\delta\sigma(T, \mu) = \sigma(T, \mu) - \sigma(T, 0). \quad (12)$$

The Polyakov-loop operator is defined by

$$L(\mathbf{x}) = \frac{1}{N_c} \prod_{t=1}^{N_t} U_4(\mathbf{x}, t) \quad (13)$$

with link variables $U_\mu \in \text{SU}(2)$. The average value Φ of L is related to the single static-quark free energy F_q as

$$\Phi = \langle L \rangle \sim e^{-F_q/T}. \quad (14)$$

The Polyakov loop Φ is an order parameter of the confinement/deconfinement transition if m is infinitely large. In fact, if F_q is finite (infinite), Φ is finite (zero). The symmetry associated with the confinement/deconfinement transition is Z_2 symmetry under the transformation

$$U_4(\mathbf{x}, t) \rightarrow z_2(t)U_4(\mathbf{x}, t), \quad (15)$$

where z_2 is the element of Z_2 group that depends only on the temporal coordinate t . Pure gauge action is invariant under this transformation while L is not. Hence, $\Phi = \langle L \rangle$ is an order parameter of Z_2 symmetry breaking. Effects of dynamical quark break Z_2 symmetry explicitly and Φ is not a proper order parameter of confinement/deconfinement transition. As mentioned in the previous section, however, at $\theta = (2k+1)\pi/2$ the system is symmetric under the $\mathcal{C}Z_2$ transformation [25]. Hence, Φ becomes an order parameter of the combined symmetry there.

III. PNJL MODEL

Two-color QCD has Pauli-Gürsey symmetry in the limit of $m = \mu = 0$ [47, 48]. The PNJL Lagrangian of QC₂D is so constructed as to have the symmetry and is given by [25, 49]

$$\begin{aligned} \mathcal{L} = & \bar{q}(i\gamma^\nu D_\nu - m)q \\ & + G[(\bar{q}q)^2 + (\bar{q}i\gamma_5\bar{\tau}q)^2 + |q^T C i\gamma_5\tau_2 t_2 q|^2] \\ & + G_8[(\bar{q}q)^2 + (\bar{q}i\gamma_5\bar{\tau}q)^2 + |q^T C i\gamma_5\tau_2 t_2 q|^2]^2 \\ & - G_v(\bar{q}\gamma^\nu q)^2 - \mathcal{U}(\Phi), \end{aligned} \quad (16)$$

where q , m , t_i , τ_i , G , G_8 , G_v are the two-flavor quark fields, the current quark mass, the Pauli matrices in the color and the flavor spaces, the coupling constants of the scalar-type four-quark interaction, the scalar-type eight-quark interaction and the vector-type four-quark interaction, respectively. The potential \mathcal{U} is a function of Φ .

The mean-field approximation leads us to the thermodynamical potential Ω as [49]

$$\begin{aligned} \Omega = & -2N_f \int \frac{d^3p}{(2\pi)^3} \sum_{\pm} [E_p^{\pm} + E_p^{-} + T(\ln f^{-} + \ln f^{+})] \\ & + U + \mathcal{U}(\Phi) \end{aligned} \quad (17)$$

with

$$f^{\pm} = 1 + 2\Phi e^{-\beta E_p^{\pm}} + e^{-2\beta E_p^{\pm}}, \quad (18)$$

$$\begin{aligned} U = & G(\sigma^2 + \tilde{\Delta}^2) + 3G_8(\sigma^2 + \tilde{\Delta}^2)^2 \\ & - G_v n_q^2, \end{aligned} \quad (19)$$

where N_f is the number of flavors, and $\tilde{\Delta} = |\langle q^T C i\gamma_5\tau_2 t_2 q \rangle|$ is the diquark condensate. The E_p^{\pm} are defined by

$$E_p^{\pm} = \text{sgn}(E_p \pm \tilde{\mu}) \sqrt{(E_p \pm \tilde{\mu})^2 + \Delta^2}, \quad (20)$$

where $E_p \equiv \sqrt{p^2 + M^2}$ with the effective quark mass $M \equiv m - 2G\sigma - 4G_8\sigma(\sigma^2 + \tilde{\Delta}^2)$, $\tilde{\mu} = \mu - 2G_v n_q$, $\Delta = -2G\tilde{\Delta}$, and $\text{sgn}(E_p \pm \tilde{\mu})$ is the sign function. When $m = \mu = 0$, Ω becomes invariant under the rotation in σ - $\tilde{\Delta}$ plane as a consequence of Pauli-Gürsey symmetry. Usually, G and G_8 are assumed to be constant. However, they may depend on Φ [50]. Here we consider Φ -dependent G and G_8 defined by

$$G \equiv G_0(1 - \alpha\Phi^2), \quad G_8 \equiv G_{8,0}(1 - \alpha\Phi^2), \quad (21)$$

where G_0 , $G_{8,0}$ and α are constant parameters. In the Polyakov gauge, Φ is given by

$$\Phi = \frac{1}{2}(e^{i\phi} + e^{-i\phi}) = \cos(\phi), \quad (22)$$

for real number ϕ . Following Ref. [49], we take the Polyakov-loop effective potential of the form

$$\frac{\mathcal{U}(\Phi)}{T} = -b \left[24e^{-a/T}\Phi^2 + \ln(1 - \Phi^2) \right]. \quad (23)$$

As will be mentioned in the next section, we determine these parameters to reproduce LQC₂D data on n_q at $\beta = 0.75$ and the pseudo-critical temperature $T_{c0} = 146$ MeV at $\mu = 0$.

Because this model is nonrenormalizable and the first two terms in Ω are divergent. We then regularize them by introducing a three-dimensional momentum cutoff as

$$\int \frac{d^3p}{(2\pi)^3} \rightarrow \frac{1}{2\pi^2} \int_0^\Lambda dp p^2. \quad (24)$$

The mean fields $X = \sigma, \Delta, n_q, \Phi$ are determined from the stationary conditions

$$\frac{\partial\Omega}{\partial X} = 0. \quad (25)$$

We found that Δ is always zero at the temperature and the density we treat in this paper.

There are six parameters in the NJL sector of the PNJL model. The values of m , G_0 , $G_{8,0}$ and Λ are chosen to reproduce the vacuum property in LQC₂D simulations. The values of G_v and α are chosen to reproduce LQC₂D data on n_q ; see Sec. IV. Table II shows the parameter set used in this paper.

$m_{\text{ps}}[\text{MeV}]$	$M_0[\text{MeV}]$	$G_0[\text{GeV}^{-2}]$	$G_{8,0}[\text{GeV}^{-8}]$
616	354	4.6	60
G_v/G_0	$\Lambda[\text{MeV}]$	$m[\text{MeV}]$	α
0.15	700	110	0.2

TABLE II: Parameters of PNJL model. M_0 is the effective quark mass at vacuum.

IV. ANALYTICAL CONTINUATION OF PHYSICAL QUANTITIES

A. Analytical continuation

In this section, we show the numerical results of LQC₂D simulations and perform the analytical continuation of physi-

cal quantities from the region at imaginary μ to the region at real μ , and finally examine the validity of analytical continuation.

Figure 1 shows T dependence of Φ for several values of $\hat{\mu} \equiv \mu/T$ from $i\pi/2$ to 1.2. For all the cases except $\hat{\mu}^2 = (i\pi/2)^2 = -(\pi/2)^2$, Φ increases smoothly as T goes up. The deconfinement transition is thus crossover there. This property is the same as in QCD with three colors [51]. For each $\hat{\mu}^2$, the pseudo-critical temperature $T_c(\hat{\mu}^2)$ (or $\beta_c(\hat{\mu}^2)$) is defined by the temperature where the susceptibility of Φ becomes maximum. It is found from LQC₂D simulations at $\hat{\mu} = 0$ that $T_{c0} \equiv T_c(0) = 146$ MeV. As for $\hat{\mu}^2 = (i\pi/2)^2$, Φ is almost zero below $T = 1.12T_{c0}$ and increases rapidly above $T = 1.14T_{c0}$. This indicates that the transition is the second order. As mentioned in Sec. I, at $\hat{\mu} = i\theta = i\pi/2$ the system is symmetric under the CZ_2 transformation, and Φ as an order parameter of spontaneous breaking of the symmetry is zero below T_{RW} and finite above T_{RW} . Therefore, T_{RW} is located somewhere in a range of $T = 1.12 \sim 1.14T_{c0}$.

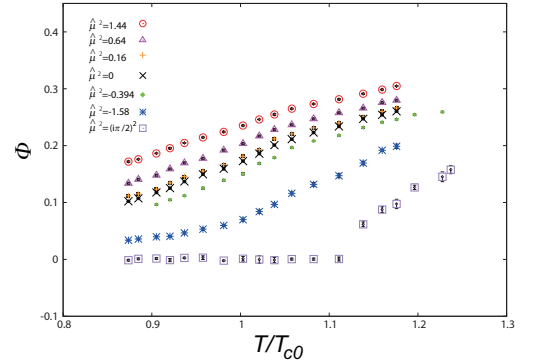


Fig. 1: LQC₂D results on T dependence of Φ for several values of $\hat{\mu}^2$

Figure 2 shows the pseudo-critical line $\beta_c(\hat{\mu}^2)$ in $\hat{\mu}^2$ - β plane, and it is found that $\beta_c(\hat{\mu}^2)$ decreases as $\hat{\mu}^2$ increases. The value of $T_c(\hat{\mu}^2)$ at $\hat{\mu}^2 = (i\pi/2)^2$ determined from $\beta_c((i\pi/2)^2)$ is $1.16T_{c0}$ and slightly larger than T_{RW} estimated above. This inconsistency is understood as follows. In our calculations, β dependence of the Polyakov-loop susceptibility is calculated every 0.01 for each value of $\hat{\mu}^2$, and the data are fitted with a Gaussian function and the value of $\beta_c(\hat{\mu}^2)$ is evaluated as the point where the Gaussian function becomes maximum. The Gaussian fitting is, however, not valid in the vicinity of singular point (the endpoint of RW phase transition). We then adopt the value $1.12 \sim 1.14T_{c0}$ as T_{RW} .

Now we test the analytic continuation from imaginary μ to real μ for the cases of $\beta = 0.75, 0.70, 0.65$ and 0.60 that correspond to $T/T_{c0} = 1.18, 1.06, 0.96, 0.88$, respectively. The system is in the deconfinement (D) phase at $\beta = 0.75$, while it is in the confinement (C) phase at $\beta = 0.60$. At $\beta = 0.70$ (0.65), the system is in the C-phase when $\hat{\mu}^2 < -1.15$ (1.35) and in the D-phase when $\hat{\mu}^2 > -1.15$ (1.35). For each temperature, we then use different analytic functions

as explained below [22, 23, 52].

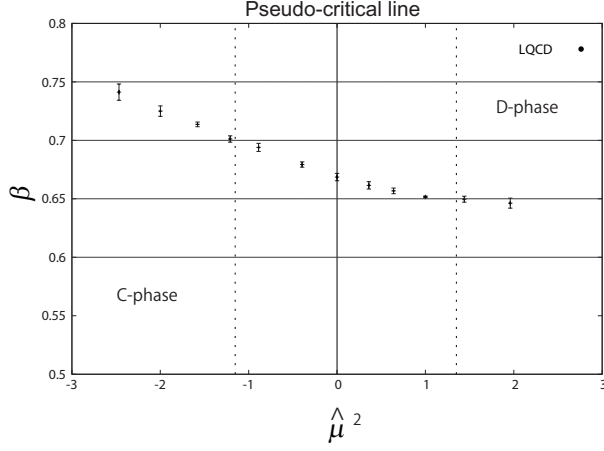


Fig. 2: Pseudo-critical line of deconfinement transition in $\hat{\mu}^2$ - β plane. In each of thin horizontal solid lines, β is constant, and in each of thin vertical dotted lines $\hat{\mu}^2$ is constant. At $\beta = 0.70$, the left hand side of the left thin vertical dotted line belongs to the C-Phase, and the right side does to the D-phase. At $\beta = 0.65$, the left hand side of the right thin vertical dotted line corresponds to the C-Phase, and the right side does to the D-phase. Note that $\beta_c(0) = 0.67$.

1. $T_{RW} < T(\beta = 0.75)$

At this temperature, due to the existence of RW transition, physical quantities cannot be described by any continuous periodic function. Hence we use a polynomial series of the form

$$A + B\hat{\mu}^2, \quad (26)$$

or

$$A + B\hat{\mu}^2 + C\hat{\mu}^4, \quad (27)$$

for $\hat{\mu}$ -even quantities Φ and σ , where A, B, C are expansion coefficient. For a $\hat{\mu}$ -odd quantity n_q , we use

$$A\hat{\mu} + B\hat{\mu}^3, \quad (28)$$

or

$$A\hat{\mu} + B\hat{\mu}^3 + C\hat{\mu}^5. \quad (29)$$

2. $T_{c0} < T(\beta = 0.70) < T_{RW}$

At this temperature, the system is in the D-phase when $\hat{\mu}^2 > -1.15$. We then use the same polynomial series as in the case of $\beta = 0.75$, but consider only the region $-1.15 < \hat{\mu}^2 \leq 0$ as a fitting range. For Φ and σ , we use only the quadratic function (26), since the number of data we can use is small.

3. $T(\beta = 0.60, 0.65) < T_{c0}$

At this temperature, the system is in the C-phase at imaginary and zero $\hat{\mu}$. Hence, it is expected that physical quantities can be well described by continuous periodic functions. Since $\Phi(\theta)$ is θ -even and has a periodicity of 2π in $\theta = \text{Im}(\hat{\mu})$, we use the following Fourier series

$$A \cos(\theta), \quad (30)$$

or

$$A \cos(\theta) + B \cos(3\theta), \quad (31)$$

for Φ . Note that the terms of $\cos(2\theta)$ and $\cos(4\theta)$ as well as the constant term are excluded, since $\Phi(\pi/2 + \theta') = -\Phi(\pi/2 - \theta')$ for any θ' . The chiral condensate $\sigma(\theta)$ is a θ -even and periodic function with a period π . We then use the following Fourier series

$$A + B \cos(2\theta), \quad (32)$$

or

$$A + B \cos(2\theta) + C \cos(4\theta), \quad (33)$$

for σ . The quark number density $n_q(\theta)$ is a θ -odd and periodic function with a period π . We therefore use the following Fourier series

$$A \sin(2\theta), \quad (34)$$

or

$$A \sin(2\theta) + B \sin(4\theta), \quad (35)$$

for n_q . Note that, in the case of $\beta = 0.65$, the system is in the D-phase when $\hat{\mu}^2 > 1.35$. Hence, the Fourier series in which the coefficients are determined from LQCD data at imaginary $\hat{\mu}$ and zero $\hat{\mu} = 0$ may not work there.

4. Pseudo-critical line

The pseudo-critical line $\beta_c(\hat{\mu}^2)$ is $\hat{\mu}$ -even. We then use the polynomial series (26) and (27).

B. Quark number density

First we consider the analytic continuation of n_q . Figure 3 shows $\hat{\mu}^2$ dependence of $(n_q/T)^2$ for several values of T . The analytic continuation has errors coming from LQCD data at zero and imaginary $\hat{\mu}$. We then plot the upper and lower bounds of analytic continuation by a pair of same lines. The $(n_q/T)^2$ are smooth at $\hat{\mu} = 0$, as expected. This is true for $\delta\sigma$ and Φ , as shown later. This guarantees that the analytic continuation from imaginary $\hat{\mu}$ to real $\hat{\mu}$ is possible.

At $\beta = 0.75$ ($T/T_{c0} = 1.18$), the system is in the D-phase and hence the polynomial series is used. The coefficients determined from LQCD data at imaginary μ are tabulated in Table III (a) of Appendix A. The polynomial series up to $\hat{\mu}^3$ well

reproduces LQC₂D data in a wide range of $0 \leq \hat{\mu}^2 \leq (1.2)^2$. Note that the analytic function deviates from LQC₂D data near the first-order RW phase transition present at $T > T_{RW}$ and $\hat{\mu}^2 = -(\pi/2)^2$.

At $\beta = 0.70$ ($T/T_{c0} = 1.06$), the system is in the C-phase when $\hat{\mu}^2 < -1.15$, while it is in the D-phase otherwise. Hence, we use only seven data in a range of $\hat{\mu}^2 = -1.15 \sim 0$ to determine the coefficients of polynomial series. The coefficients of the function are tabulated in Table III (b) of Appendix A. LQC₂D data calculated at real $\hat{\mu}$ lie between the upper and the lower bounds of the polynomial series up to $\hat{\mu}^3$ in a wide range of $0 \leq \hat{\mu}^2 \leq (1.2)^2$.

At $\beta = 0.65$ ($T/T_{c0} = 0.96$), the system is in the C-phase when $\hat{\mu}^2 < 1.35$, while it is in the D-phase otherwise. Hence, we use the Fourier series. The coefficients of the function are tabulated in Table III (c) of Appendix A. The analytic functions fail to reproduce LQC₂D data calculated at real $\hat{\mu}$ when $\hat{\mu}^2 \geq 0.4$. The large deviation at large $\hat{\mu}^2$ may be originated in the fact that the system is in the D-phase there and the Fourier series may not be valid anymore.

At $\beta = 0.60$ ($T/T_{c0} = 0.88$), the system is in the C-phase. Therefore, we use the Fourier series. The coefficients of the function are tabulated in Table III (d) of Appendix A. The Fourier series up to the term $\sin(2\theta)$ ($\sin(4\theta)$) are consistent with LQC₂D data calculated at real $\hat{\mu}$ in a wide range $0 \leq \hat{\mu}^2 < 0.8$ ($0 \leq \hat{\mu}^2 \leq (1.2)^2$).

Comparing four cases of T/T_{c0} with each other, one can see that the analytic continuation is reasonable at higher T/T_{c0} where the system is always in the D-phase when $\hat{\mu}^2$ varies from $-(\pi/2)^2$ to $(1.2)^2$ and at lower T/T_{c0} where the system is always in the C-phase when $\hat{\mu}^2$ varies from $-(\pi/2)^2$ to $(1.2)^2$. Near $T/T_{c0} = 1$, however, the system changes from the C-phase to the D-phase as $\hat{\mu}^2$ varies from $-(\pi/2)^2$ to a positive value. A simple analytic function cannot follow the complicated change properly. Therefore, the analytic continuation is reasonable except for the vicinity of deconfinement crossover.

C. Chiral condensate

Figure 4 shows $\hat{\mu}^2$ dependence of $\delta\sigma$ for several values of T . Again, the upper and lower bounds of analytic continuation are shown by a pair of same lines; see Table III for the coefficients of analytic function determined from LQC₂D data at imaginary μ . As for $\delta\sigma$, one can make the same discussion as in Sec. IV B for n_q , as shown below, although the analytic function taken in the C-phase is a cosine function.

At $\beta = 0.75$ ($T/T_{c0} = 1.18$), the polynomial series up to $\hat{\mu}^2$ well reproduces LQC₂D data calculated at real $\hat{\mu}$ in a wide range of $0 \leq \hat{\mu}^2 \leq (1.2)^2$. At $\beta = 0.70$ ($T/T_{c0} = 1.06$), the system is in the C-phase when $\hat{\mu}^2 < -1.15$, while it is in the D-phase otherwise. Hence, we can use only three data in a range of $\hat{\mu}^2 = -1.15 \sim 0$ to determine the coefficients of analytic function and then use the quadratic function only. The function is consistent with LQC₂D data calculated at real $\hat{\mu}$ in a wide range of $0 \leq \hat{\mu}^2 \leq (1.2)^2$.

At $\beta = 0.65$ ($T/T_{c0} = 0.96$), the system is in the C-phase

when $\hat{\mu}^2 < 1.35$, while it is in the D-phase otherwise. Hence, we use the Fourier series. The analytic functions is not consistent with LQC₂D data calculated at real $\hat{\mu}$ when $\hat{\mu}^2 > 0.4$. As mentioned in the case of n_q , this failure at large $\hat{\mu}$ may show that the system is in the D-phase there and the Fourier series becomes less reliable. At $\beta = 0.60$ ($T/T_{c0} = 0.88$), the system is in the C-phase. Hence, we use the Fourier series. The analytic functions are consistent with LQC₂D data calculated at real $\hat{\mu}$ in a range of $0 \leq \hat{\mu}^2 < 0.8$

D. Polyakov loop

Figure 5 shows $\hat{\mu}^2$ dependence of Φ at several values of T . Again, the upper and the lower bounds of analytic continuation are shown by a pair of same lines; see Table III for the coefficients of analytic function. As for Φ , one can make the same discussion qualitatively as in Sec. IV C for $\delta\sigma$.

E. Pseudo-critical line

Figure 6 shows the transition line of deconfinement crossover in $\hat{\mu}^2$ - β plane. The pseudo-critical $\beta_c(\hat{\mu}^2)$ at $\hat{\mu}^2 = 0$ is about 0.67. We consider the polynomial series the coefficients of which are obtained from LQC₂D data at imaginary μ and tabulated in Table IV of Appendix A. The polynomial series up to $\hat{\mu}^2$ well reproduces LQC₂D data at $0 \leq \hat{\mu}^2 < 0.8$, but deviates at $\hat{\mu}^2 > 0.8$. The polynomial series up to $\hat{\mu}^4$ is consistent with LQC₂D data even at $\hat{\mu}^2 > 0.8$, but the difference between the upper and lower bounds of analytic continuation is large. Therefore, we should consider that the analytic continuation of the pseudo-critical line is reasonable at $0 \leq \hat{\mu}^2 < 0.8$.

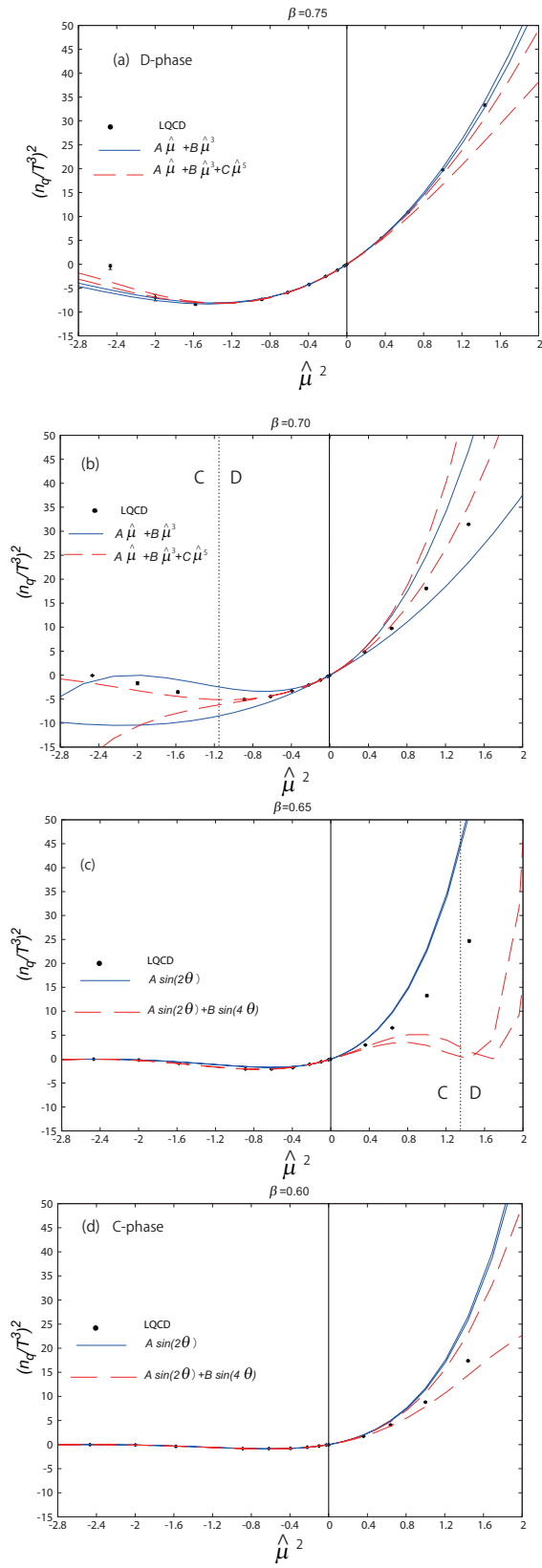


Fig. 3: $\hat{\mu}^2$ dependence of n_q at (a) $\beta = 0.75$ ($T/T_{c0} = 1.18$), (b) $\beta = 0.70$ ($T/T_{c0} = 1.06$), (c) $\beta = 0.65$ ($T/T_{c0} = 0.96$) and (d) $\beta = 0.60$ ($T/T_{c0} = 0.88$). The dots with error bars are the results of LQC₂D data. The solid and dashed lines represent the results of analytic continuation in which two types of analytic functions are taken as shown by legends. The upper and lower bounds of analytic continuation is shown by a pair of same lines. Characters C and D denote confinement and deconfinement phases, respectively.

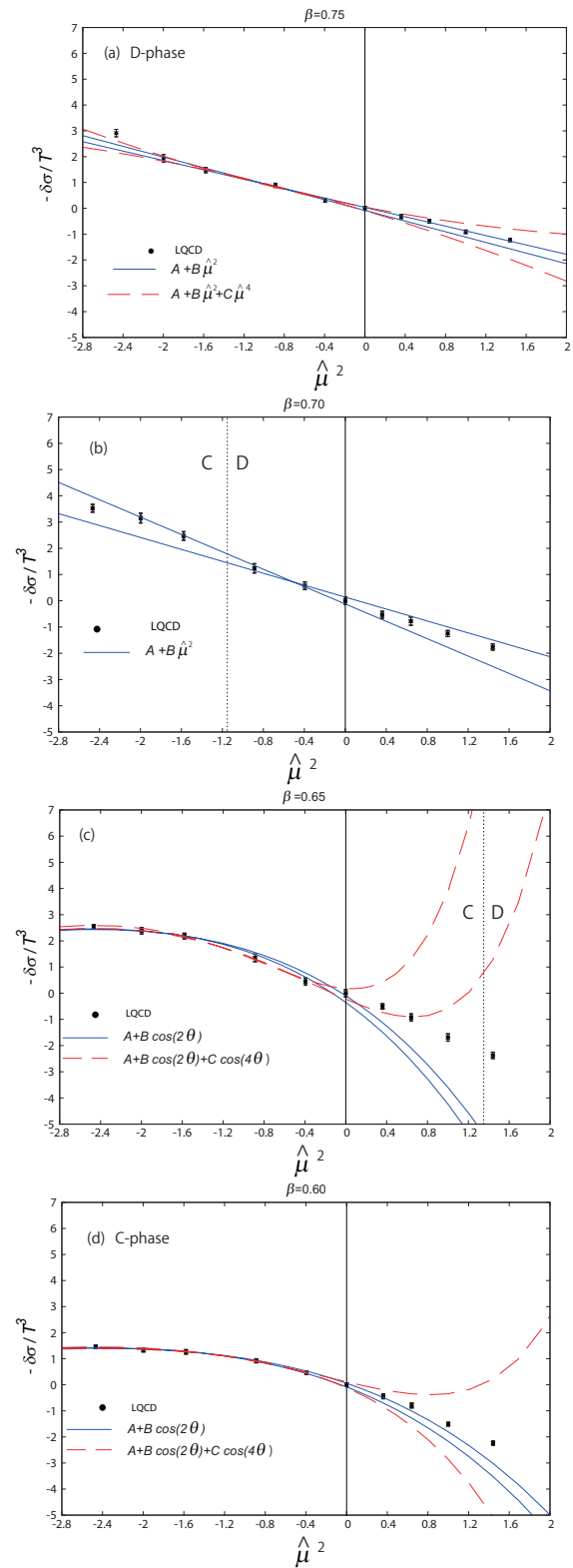


Fig. 4: $\hat{\mu}^2$ -dependence of σ at (a) $\beta = 0.75$ ($T/T_{c0} = 1.18$) (b) $\beta = 0.70$ ($T/T_{c0} = 1.06$) (c) $\beta = 0.65$ ($T/T_{c0} = 0.96$) (d) $\beta = 0.60$ ($T/T_{c0} = 0.88$). For the definition of dots, lines and characters, see the caption of Fig. 3.

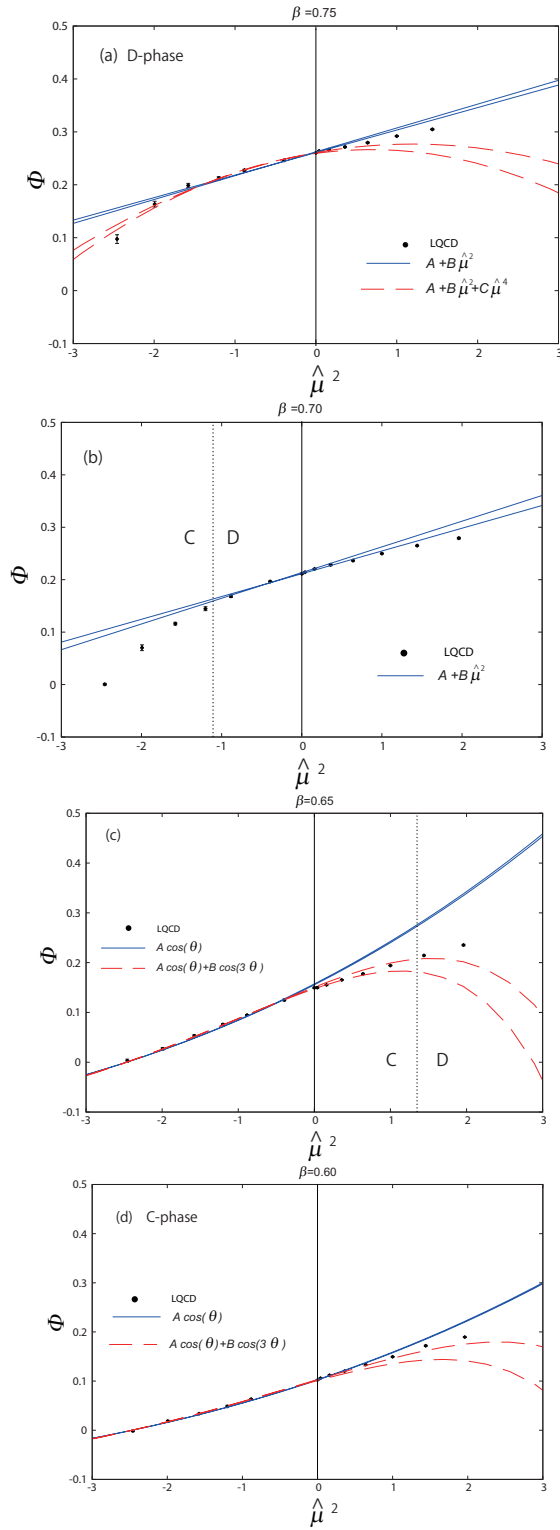


Fig. 5: $\hat{\mu}^2$ -dependence of Φ at (a) $\beta = 0.75$ ($T/T_{c0} = 1.18$), (b) $\beta = 0.70$ ($T/T_{c0} = 1.06$), (c) $\beta = 0.65$ ($T/T_{c0} = 0.96$) and (d) $\beta = 0.60$ ($T/T_{c0} = 0.88$). For the definition of dots, lines and characters, see the caption of Fig. 3.

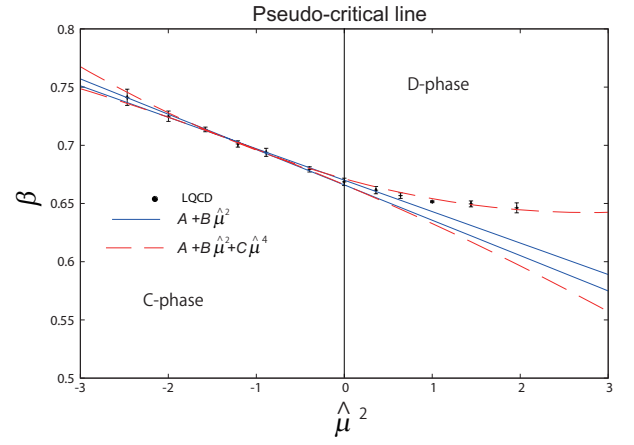


Fig. 6: Pseudo-critical line of deconfinement crossover in $\hat{\mu}^2$ - β plane. Note that $\beta_c(0) = 0.67$. For the definition of dots, lines and characters, see the caption of Fig. 3.

V. COMPARISON OF PNJL MODEL WITH LQC₂D DATA

A. Parameter setting

In this section, we compare results of the PNJL model with LQC₂D data to test the validity of the model. For this purpose, we first fix the parameters of the model. For the NJL sector, the parameters have already been determined in Sec. III. We then fix the remaining parameters a , b , α and G_v here.

Figure 7 shows T dependence of n_q divided by its Stephan-Boltzmann (SB) limit n_{SB} for several values of $\hat{\mu}^2$ from $-(\pi/2)^2$ to $(1.2)^2$. LQC₂D results include a lattice artifact due to finite volume and spacing. The artifact is expected to be reduced in n_q/n_{SB} . For all the values of $\hat{\mu}^2$, the ratio n_q/n_{SB} increases as T increases.

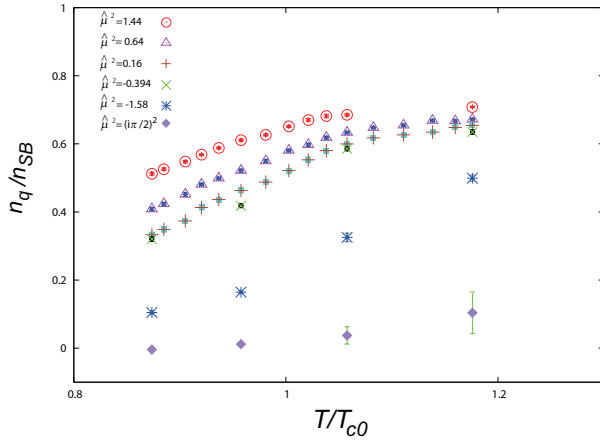


Fig. 7: T dependence of n_q/n_{SB} for several values of $\hat{\mu}^2$. Six cases of $\hat{\mu}^2 = (\frac{i\pi}{2})^2, -1.58, -0.394, 0.16, 0.64, 1.44$ are shown from the bottom.

Now we determine the parameters a , b , α and G_v from n_q at the highest T in the present analyses, i.e., at $\beta = 0.75$ ($T/T_{c0} = 1.18$). One reason is that the PNJL model is essentially a model for quark dynamics and it may work better at higher T than at lower T . Another reason is that n_q does not need the renormalization and is sensitive to the value of G_v .

Figure 8 shows $\hat{\mu}^2$ dependence of n_q/n_{SB} at $\beta = 0.75$ at imaginary μ . As $\hat{\mu}^2$ decreases, the chiral symmetry breaking becomes stronger and the effective quark mass M becomes larger [34], so that n_q/n_{SB} decreases. We searched the parameters a , b , α and G_v so as to reproduce both the result of Fig. 8 and $T_{c0} = 146$ MeV. The parameters thus obtained are shown in Table II of Sec. III. It is interesting that the vector interaction is needed to reproduce LQC₂D results data at imaginary μ . In fact, the model with $G_v = 0.15G_0$ (solid line) yields better agreement with LQC₂D data than the model with $G_v = 0$ (dotted line). This method may work as a way of determining the vector coupling also in realistic QCD with three colors [36, 40, 41].

T dependence of Φ is shown in Fig. 9 for three cases of $\hat{\mu}^2 = -(\pi/2)^2, 0, 1.44$. Since the renormalization is needed

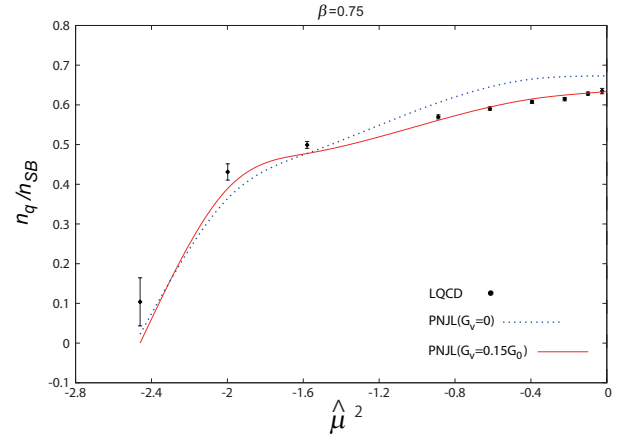


Fig. 8: $\hat{\mu}^2$ dependence of n_q/n_{SB} at $\beta = 0.75$ at imaginary μ . The dots with error bars are the results of LQC₂D data. The solid (dotted) line is the result of PNJL model with $G_v/G_0 = 0.15$ (0).

for Φ , we multiply the PNJL results by a factor 0.304 to reproduce LQC₂D results at $\hat{\mu} = 0$ and $T = T_{c0}$. The renormalized PNJL results (solid lines) reproduce LQC₂D data qualitatively, except for the vicinity of the first-order RW phase transition at $T > T_{RW} \approx 1.13T_{c0}$ and $\hat{\mu}^2 = -(\pi/2)^2$. The value of T_{RW} is 178 MeV in the PNJL model, but 163 ~ 166 MeV in LQC₂D data. In the present model, it is quite difficult to reproduce LQC₂D values of T_{c0} and T_{RW} simultaneously. A fine tuning of the Polyakov potential $\mathcal{U}(\Phi)$ may be necessary.

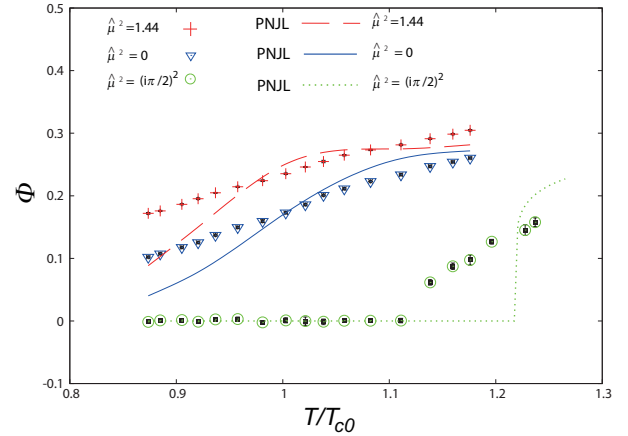


Fig. 9: T dependence of Φ for three values of $\hat{\mu}^2$. The dots represent LQC₂D data. The solid (dotted, dashed) line represents the PNJL results at $\hat{\mu}^2 = 0$ ($-(\pi/2)^2$), 1.44). The PNJL results are multiplied by the normalization factor 0.304.

B. Quark number density

Figure 10 shows $\hat{\mu}^2$ dependence of n_q/n_{SB} at $\beta = 0.75$ ($T/T_{c0} = 1.18$). As mentioned in the previous subsec-

tion, we have used LQC₂D on n_q/n_{SB} at $\beta = 0.75$ and imaginary μ to determine the parameter set of the PNJL model. The parameter set thus determined well reproduces LQC₂D data even at real μ . This ensures the assumption that the PNJL model is valid at high T . Also note that the PNJL model with $G_v = 0$ fails to reproduce LQC₂D data at real μ , while the PNJL model with G_v agrees with the LQC₂D data even at real μ . The imaginary chemical potential matching approach is thus a promising method.

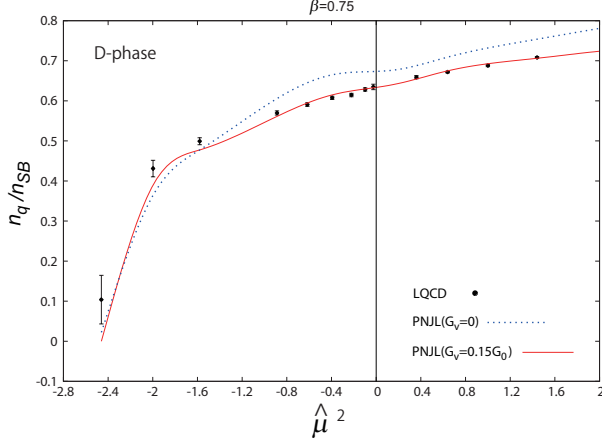


Fig. 10: $\hat{\mu}^2$ -dependence of n_q/n_{SB} for $\beta = 0.75$ ($T/T_{c0} = 1.18$). The dots with error bars are the results of LQC₂D data, while the solid (dotted) line corresponds to the result of PNJL model with $G_v/G_0 = 0.15$ (0). Note that n_q/n_{SB} at $\hat{\mu} = 0$ is defined by $\lim_{\hat{\mu} \rightarrow 0} n_q/n_{SB}$.

Figure 11 shows the same as Fig. 10 but for $\beta = 0.70$ ($T/T_{c0} = 1.06$). On the left (right) side of the vertical thin dotted line, the system is in the C-phase (D-phase). The PNJL result (solid line) underestimates LQC₂D data sizably in the C-phase. To improve this, we consider free “baryons” and assume that the baryons have the same degrees of freedom as PS mesons, and add a contribution of free baryon gas to the PNJL results. Note that, in QC₂D, the baryon is a boson consisting of two quarks. According to Ref. [18], the scalar baryon with the same degree of freedom as the PS meson has almost the same mass as the PS meson. Hence, we use the baryon mass $m_B = m_{ps} = 616\text{MeV}$. In this way, the baryon contribution to n_q is given by

$$n_{q,B} = 2g \int \frac{d^3p}{(2\pi)^3} \left[\frac{1}{e^{\beta(E_B - 2\mu)} - 1} - \frac{1}{e^{\beta(E_B + 2\mu)} - 1} \right], \quad (36)$$

where $E_B = \sqrt{p^2 + m_B^2}$, $g = 3$ is the degree of freedom and the factor 2 in front of g comes from the fact that the baryon is composed of two quarks. This modification improves agreement with LQC₂D particularly in the C-phase, but not in the D-phase. This implies that baryons disappear in the D-phase at least partially.

Figure 12 shows the same as Fig. 10 but for $\beta = 0.65$ ($T/T_{c0} = 0.96$). The system is in the C-phase on the

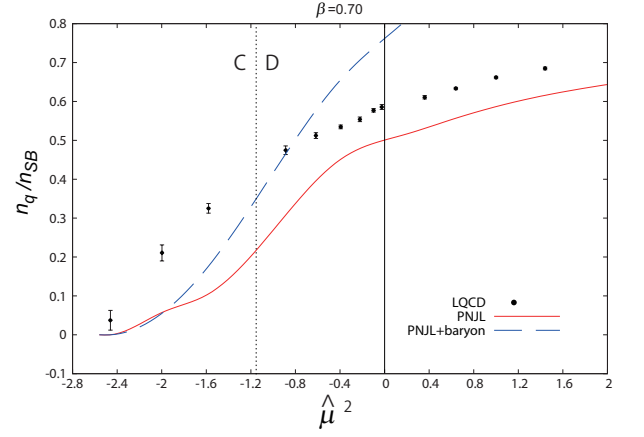


Fig. 11: $\hat{\mu}^2$ -dependence of n_q/n_{SB} for $\beta = 0.70$ ($T/T_{c0} = 1.06$). The dots with error bars are the results of LQC₂D data, while the solid (dashed) line corresponds to the result of the PNJL model (the PNJL+baryon model). On the left (right) side of the thin dotted line, the system is in the C-phase (D-phase).

left side of the thin dotted line, but in the D-phase on the right side. Again, the PNJL model underestimates LQC₂D in the C-phase, but the PNJL+baryon model almost reproduces the LQC₂D data in the C-phase, although the latter model overshoots LQC₂D data in the D-phase. Thus, the baryon may disappear in the D-phase.

More precisely, the PNJL+baryon model overestimates LQC₂D data also in the C-phase near the thin dotted line. This fact may imply that a repulsive force works between baryons there. It is well known that such a repulsive force suppresses the baryon number density in realistic nuclear matter.

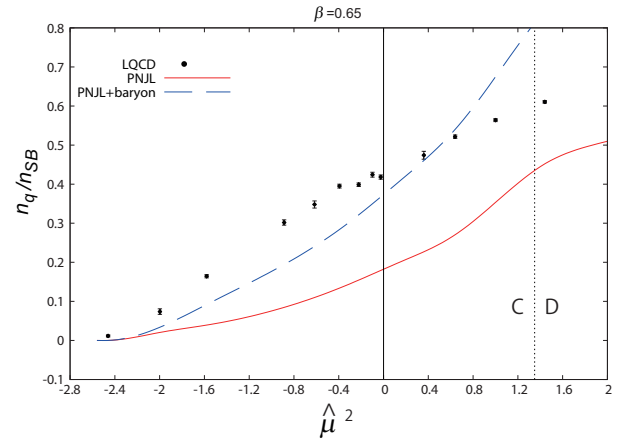


Fig. 12: $\hat{\mu}^2$ -dependence of n_q/n_{SB} for $\beta = 0.65$ ($T/T_{c0} = 0.96$). For the definition of lines, see the caption of Fig. 11.

Figure 13 shows the same as Fig. 10 but for $\beta = 0.60$ ($T/T_{c0} = 0.88$). The system is in the C-phase and the PNJL model largely underestimates LQC₂D data, but it is improved by the PNJL+baryon model. We can therefore conclude that baryon effects play an important contribution to n_q ,

whenever the system is in the C-phase.

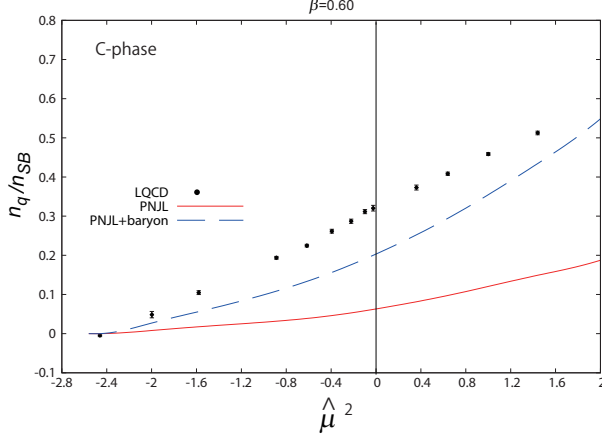


Fig. 13: $\hat{\mu}^2$ -dependence of n_q/n_{SB} for $\beta = 0.60$ ($T/T_{c0} = 0.88$). For the definition of lines, see the caption of Fig. 11.

C. Chiral condensate

As mentioned in Sec. II C, the renormalization is necessary for the chiral condensate. The PNJL results are then simply multiplied by a normalization factor 1.92 so that the results can reproduce LQC₂D data at $\beta = 0.75$ ($T/T_{c0} = 1.18$) and $\hat{\mu}^2 = (i\pi/2)^2$. This choice of normalization is natural, since the PNJL model is a quark model and is expected to be more reliable at higher T .

Figure 14 shows $\hat{\mu}^2$ dependence of $\delta\sigma$ at $\beta = 0.75$ ($T/T_{c0} = 1.18$). At this temperature, the system is in the D-phase, and the PNJL model well reproduces LQC₂D data even at real μ .

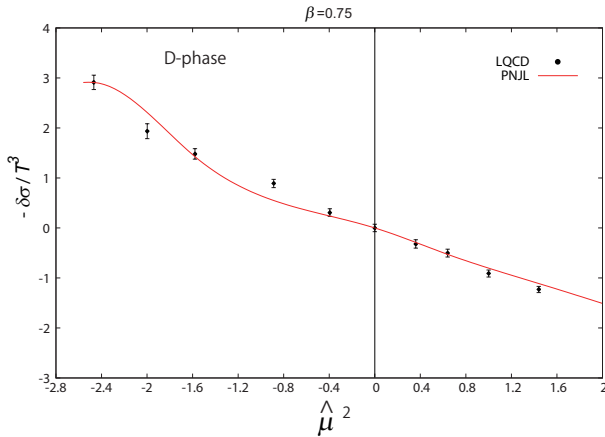


Fig. 14: $\hat{\mu}^2$ -dependence of $\delta\sigma/T^3$ at $\beta = 0.75$ ($T/T_{c0} = 1.18$). The dots with error bars are the results of LQC₂D data, while the solid line corresponds to the result of PNJL model. The PNJL result is multiplied by a normalization factor 1.92.

Figures 15 and 16 show $\hat{\mu}^2$ -dependence of $\delta\sigma$ at $\beta = 0.70$ ($T/T_{c0} = 1.06$) and $\beta = 0.65$ ($T/T_{c0} = 0.96$), respectively. On the left side of the thin vertical dotted line the system is in the C-phase, while it is in the D-phase on the right side. The PNJL model (solid line) is consistent with LQC₂D data in the D-phase, but not in the C-phase. In order to improve this disagreement in the C-phase, we add baryon effects to the PNJL model again:

$$\sigma_B = \frac{\partial m_B}{\partial m} g \int \frac{d^3 p}{(2\pi)^3} \frac{m_B}{E_B} \left[\frac{1}{e^{\beta(E_B - 2\mu)} - 1} + \frac{1}{e^{\beta(E_B + 2\mu)} - 1} \right], \quad (37)$$

where we assume

$$\frac{\partial m_B}{\partial m} = 2, \quad (38)$$

since a naive constituent quark model gives this value. As shown in Figs 15 and 16, the PNJL+baryon model (dashed line) is more consistent with LQC₂D data than the PNJL model (solid line) in the C-phase, but less consistent in the D-phase. This means that baryon effects are significant only in the C-phase.

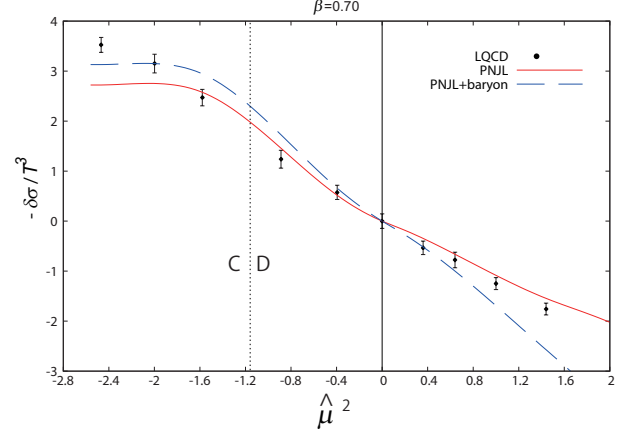


Fig. 15: $\hat{\mu}^2$ -dependence of $\delta\sigma$ at $\beta = 0.70$ ($T/T_{c0} = 1.06$). The dots with error bars are the results of LQC₂D data, while the solid (dashed) line corresponds to the results of the PNJL (PNJL+baryon) model. The model results are multiplied by a normalization factor 1.92. The system is in the C-phase on the left side of the thin vertical dotted line, but in the D-phase on the right side.

Figure 17 shows $\hat{\mu}^2$ -dependence of $\delta\sigma$ at $\beta = 0.60$ ($T/T_{c0} = 0.88$). At this temperature, the system is in the C-phase. The PNJL+baryon model (dashed line) yields better agreement with LQC₂D than the PNJL model (solid line) in the whole region of $\hat{\mu}^2$; note that $\delta\sigma$ is always zero at $\hat{\mu} = 0$ by the definition (12). Thus, baryon effects are important in the C-phase not only for n_q/n_{SB} but also for $\delta\sigma$.

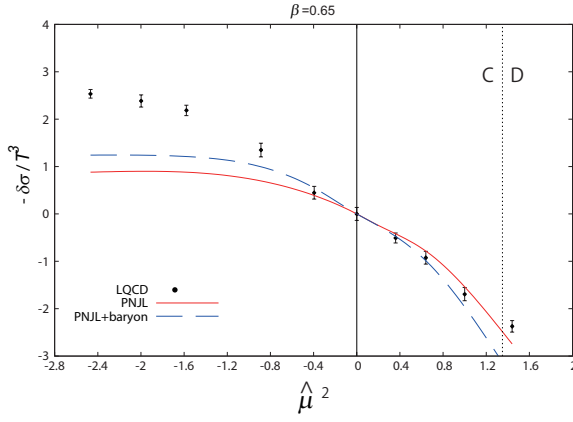


Fig. 16: $\hat{\mu}^2$ -dependence of $\delta\sigma$ at $\beta = 0.65$ ($T/T_{c0} = 0.96$). For the definition of lines, see the caption of Fig. 15.

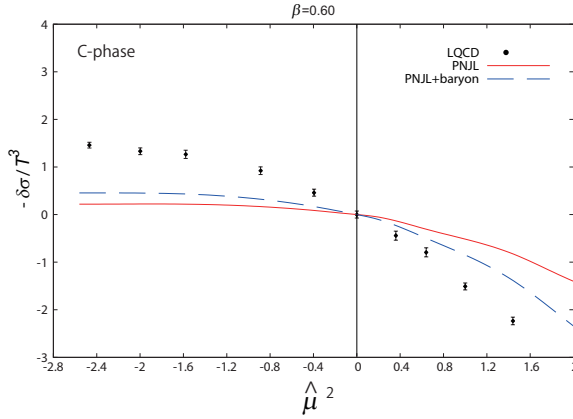


Fig. 17: $\hat{\mu}^2$ -dependence of $\delta\sigma/T^3$ at $\beta = 0.60$ ($T/T_{c0} = 0.88$). For the definition of lines, see the caption of Fig. 15.

D. Polyakov loop

Figure 18 shows $\hat{\mu}^2$ dependence of Φ at $\beta = 0.75$. As mentioned in Sec. V A, the PNJL result is multiplied by a normalization factor 0.304 for Φ . At this temperature, the system is in the D-phase. The PNJL model (solid line) well reproduces LQC₂D data except for the vicinity of the first-order RW transition.

Figures 19 and 20 show $\hat{\mu}^2$ dependence of Φ at $\beta = 0.70$ and $\beta = 0.65$, respectively. The PNJL model deviates from LQC₂D data to some extent in the C-phase except for the point at $\hat{\mu}^2 = (i\pi/2)^2$ where Z_2 symmetry restricts Φ to zero.

Figure 21 shows $\hat{\mu}^2$ -dependence of Φ at $\beta = 0.60$. At this temperature, the system is in the C-phase. The PNJL model deviates from LQC₂D data to some extent in the whole region except for the point at $\hat{\mu}^2 = (i\pi/2)^2$ where Z_2 symmetry restricts Φ to zero.

Throughout all the analyses for Φ , we can say that the PNJL model cannot reproduce LQC₂D data properly in the vicinity of RW transition and at lower T . A fine tuning of $\mathcal{U}(\Phi)$ may

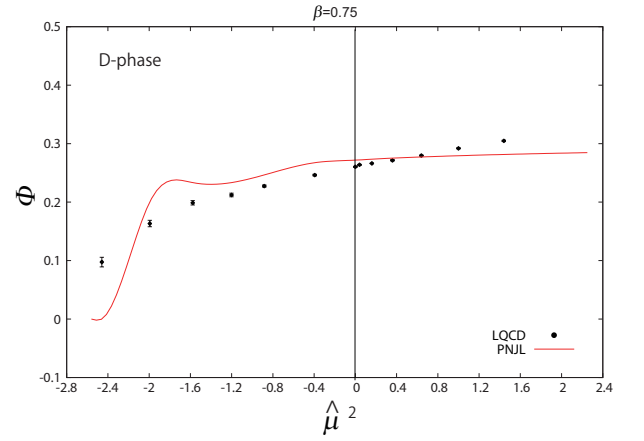


Fig. 18: $\hat{\mu}^2$ -dependence of Φ at $\beta = 0.75$ ($T/T_{c0} = 1.18$). The dots with error bars are the results of the LQC₂D data, while the solid line corresponds to the result of PNJL model. The PNJL result is multiplied by the normalization factor 0.304.

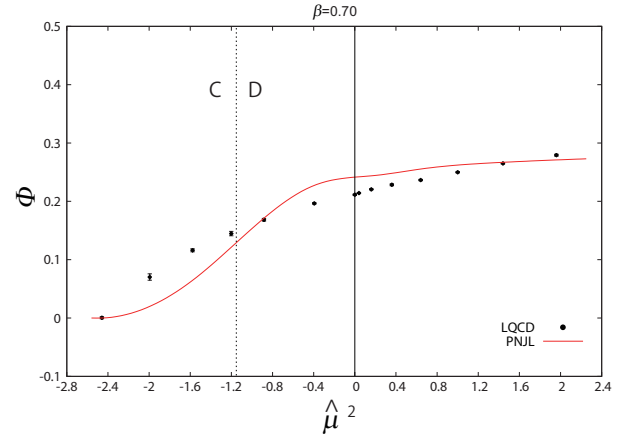


Fig. 19: $\hat{\mu}^2$ -dependence of Φ at $\beta = 0.70$ ($T/T_{c0} = 1.06$). The dots with error bars are the results of the LQC₂D data, while the solid line is the result of PNJL model. The PNJL result is multiplied by the normalization factor 0.304. The system is in the C-phase on the left side of the thin vertical dotted line, while it is in the D-phase on the right side.

be necessary to solve this problem.

E. Phase diagram

Figure 22 shows the phase diagram in $\hat{\mu}^2$ - T plane. The PNJL model (solid line) reproduces LQC₂D data well in a range of $\hat{\mu}^2 = -2 \sim 1$, but it overshoots LQC₂D data to some extent near the RW transition line and undershoots LQC₂D data in the large $\hat{\mu}^2$ region of $\hat{\mu}^2 \approx (1.2)^2$. It is an interesting question whether the PNJL model can reproduce LQC₂D data in the large $\hat{\mu}^2$ region as soon as the model is improved to reproduce LQC₂D data near the RW transition line.

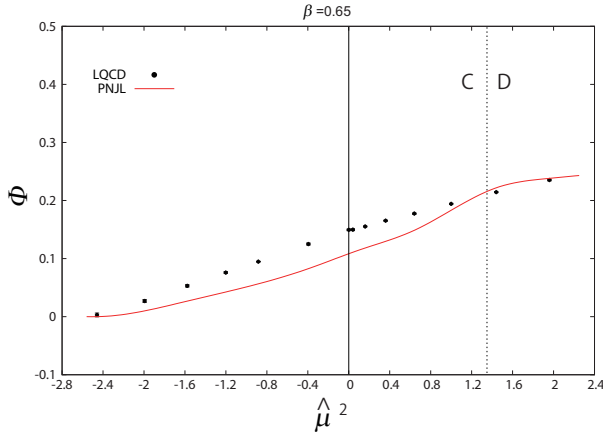


Fig. 20: $\hat{\mu}^2$ -dependence of Φ at $\beta = 0.65$ ($T/T_{c0} = 0.96$). For the definition of lines, see the caption of Fig. 19.

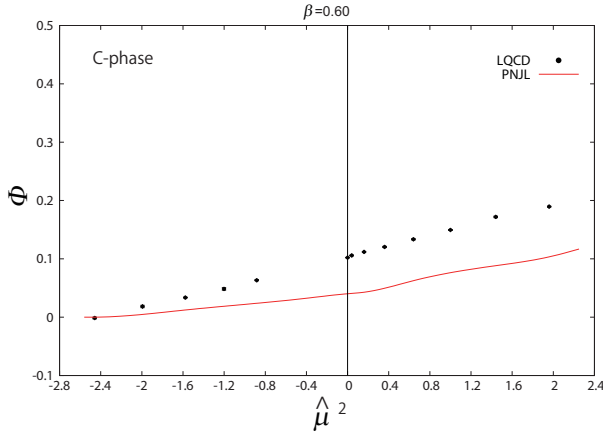


Fig. 21: $\hat{\mu}^2$ -dependence of Φ at $\beta = 0.60$ ($T/T_{c0} = 0.88$). For the definition of lines, see the caption of Fig. 18.

VI. SUMMARY

We studied the phase structure of QC_2D at both real and imaginary μ by using an $8^3 \times 4$ lattice with the renormalization-group improved Iwasaki gauge action [42, 43] and the clover-improved two-flavor Wilson fermion action [44]. The Polyakov loop, the chiral condensate and the quark number density were calculated at $0.86 \leq T/T_{c0} \leq 1.18$ and $-(\pi/2)^2 \leq \hat{\mu}^2 \leq (1.2)^2$. These quantities are smooth at $\hat{\mu} = 0$, as expected. This guarantees that the analytic continuation of physical quantities from imaginary $\hat{\mu}$ to real $\hat{\mu}$ is possible.

Accuracy of the analytic continuation was tested in Refs. [22, 23] with staggered fermions. In this paper we have made similar analyses with clover-improved Wilson fermions by assuming a polynomial series of $\hat{\mu}$ in the deconfinement phase and a Fourier series in the confinement phase, where coefficients of the series were determined at imaginary μ . As for the quark number density at $T/T_{c0} = 1.18$ corresponding to the

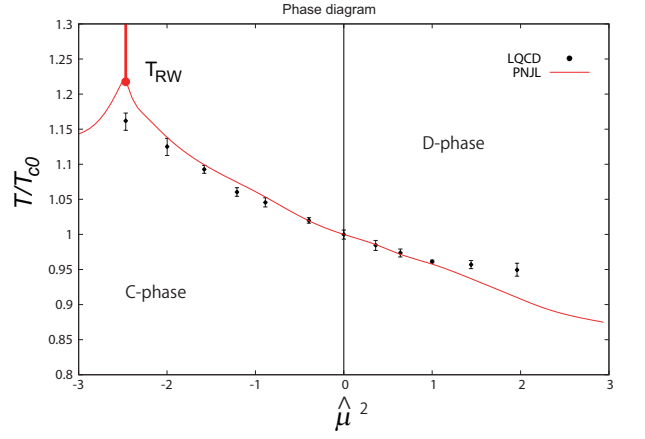


Fig. 22: Phase diagram in $\hat{\mu}^2$ - T plane. The dots with error bars represent the Pseudo-critical line of LQC_2D , while the solid line corresponds to the phase diagram of PNJL model. The vertical thick solid line is the RW transition line determined with the PNJL model.

deconfinement phase, the polynomial series up to $\hat{\mu}^3$ well reproduces LQC_2D results in a wide range of $0 \leq \hat{\mu}^2 \leq (1.2)^2$. At $T/T_{c0} = 0.88$ corresponding to the confinement phase, the results of the lowest-order Fourier series $\sin(2\theta)$ are consistent with LQC_2D results in a range of $0 \leq \hat{\mu}^2 < 0.8$. At $T/T_{c0} = 0.96$ near the deconfinement transition, it is good only in $0 \leq \hat{\mu}^2 < 0.4$. The analytic continuation is thus useful in the deconfinement and confinement regions, but less accurate in the transition region near $T/T_{c0} = 1$ where the deconfinement crossover takes place somewhere in a range of $-(\pi/2)^2 \leq \hat{\mu}^2 \leq (1.2)^2$ as $\hat{\mu}^2$ increases with T fixed. This is true for other quantities such as the Polyakov loop and the chiral condensate.

We have tested the validity of the PNJL model by comparing model results with LQC_2D ones, where the model parameters are fitted to the quark number density at $T/T_{c0} = 1.18$ and imaginary μ . As for the transition line of deconfinement crossover, the model result agrees with LQC_2D one. More precisely, the agreement is not perfect in the vicinity of RW transition line and the large- $\hat{\mu}^2$ region of $(\hat{\mu}^2) \approx (1.2)^2$. It is interesting whether the PNJL model can reproduce LQC_2D data in the large $\hat{\mu}^2$ region as soon as the model is improved to reproduce LQC_2D data near the RW transition line. A possible candidate of the improvement is a fine tuning of the Polyakov-loop potential $\mathcal{U}(\Phi)$.

In the deconfinement region of $T/T_{c0} = 1.18$, the PNJL model yields good agreement with LQC_2D data at both real and imaginary μ for the quark number density, the chiral condensate and the Polyakov loop. The agreement particularly at real μ indicates that the PNJL model is reliable in the deconfinement region. In the transition region of $T/T_{c0} \approx 1$, the agreement of the PNJL model with LQC_2D data is not perfect. As for the quark number density and the chiral condensate, however, the deviation can be reduced in the confinement area appearing at smaller $\hat{\mu}^2$ by introducing baryon degree of freedom to the PNJL model. In the deconfinement area appearing at larger $\hat{\mu}^2$, on the contrary, the model overes-

timates LQC₂D results if the baryon contribution is taken into account. This means that baryons disappear at least partially in the deconfinement area. Also in the confinement region of $T/T_{c0} = 0.88$, the baryon degree of freedom is important. As for the Polyakov loop, the disagreement between PNJL and LQC₂D results in the confinement area cannot be solved by the baryon contribution. Of course, this comes from the fact that the Polyakov-loop potential is not changed by the baryon contribution in the present framework. The improvement of PNJL model along this line is interesting.

The present analysis also shows that the vector-type four-quark interaction is necessary to explain LQC₂D data on the quark number density. This fact indicates that also in the realistic case of three colors the strength of vector-type interaction can be determined from LQCD data at imaginary μ [36, 40, 41]. Although the lattice we used is quite coarse and the number of LQC₂D data is limited, the present results surely show that the imaginary- μ matching approach [33] is a promising approach to thermodynamics of QCD at finite μ .

In this paper, we consider only the μ -region where the di-quark condensate is zero. Quantitative check of our effective model in the region [19–21] is also interesting.

Acknowledgments

T. M. and H. K. thank H. Yoneyama, A. Sugiyama and M. Tachibana for valuable comments. T. S., J.T., K.K., H.K., M.Y and A.N. are supported by JSPS KAKENHI No. 23749194, No. 25-3944, No. 26-1717, No. 26400279, No. 26400278, and Nos. 24340054 and 26610072, respectively. The numerical calculations were performed by using the NEC SX-9 and SX-8R at CMC, Osaka University, and by using the RIKEN Integrated Clusters (RICC) facility.

Appendix A: Coefficients of fitting functions for analytic continuation

We present the coefficients of analytic functions determined from LQC₂D data at imaginary μ and the $\chi^2/\text{d.o.f}$ for the fitting.

(a) $\beta = 0.75$					
observable	function	A	B	C	$\chi^2/\text{d.o.f}$
Im(n_q)	Eq.(28)	3.61014(1466)	0.84703(2265)		2.914
Im(n_q)	Eq.(29)	3.57904(1989)	0.70990(6347)	-0.08459(3657)	2.566
$\delta\sigma$	Eq.(26)	-0.07116(5561)	-1.07870(5010)		2.337
$\delta\sigma$	Eq.(27)	0.01304(8702)	-0.7336(0190)	0.1571(8106)	1.448
Φ	Eq.(26)	0.26153(70)	0.04379(12)		13.25
Φ	Eq.(27)	0.25994(73)	0.02410(310)	-0.01331(191)	4.534
(b) $\beta = 0.70$					
observable	function	A	B	C	$\chi^2/\text{d.o.f}$
Im(n_q)	Eq.(28)	3.32812(2089)	1.07313(5618)		1.077
Im(n_q)	Eq.(29)	3.34986(2818)	1.2644(1755)	0.24168(21017)	1.016
$\delta\sigma$	Eq.(26)	0.00868(13029)	-1.39546(25909)		0.018
Φ	Eq.(27)	0.21241(112)	0.04621(279)		5.590
(c) $\beta = 0.65$					
observable	function	A	B	C	$\chi^2/\text{d.o.f}$
Im(n_q)	Eq.(34)	1.31566(759)			23.80
Im(n_q)	Eq.(35)	1.44376(1216)	-0.11951(886)		4.075
$\delta\sigma$	Eq.(32)	1.1107(5784)	-1.33556(6933)		2.155
$\delta\sigma$	Eq.(33)	1.05958(6059)	-1.27686(7235)	0.19765(6969)	0.1933
Φ	Eq.(30)	0.15644(85)			7.920
Φ	Eq.(31)	0.15375(94)	-0.00461(68)		0.442
(d) $\beta = 0.60$					
observable	function	A	B	C	$\chi^2/\text{d.o.f}$
Im(n_q)	Eq.(34)	0.93599(80)			1.189
Im(n_q)	Eq.(35)	0.94541(838)	-0.01438(74)		0.877
$\delta\sigma$	Eq.(32)	0.69931(3257)	-0.71395(3973)		0.2853
$\delta\sigma$	Eq.(33)	0.69633(3414)	-0.71059(4087)	0.01373(3913)	0.3394
Φ	Eq.(30)	0.10258(38)			3.826
Φ	Eq.(31)	0.10404(52)	-0.00195(46)		0.4438

TABLE III: Coefficients of analytic functions and $\chi^2/\text{d.o.f}$ for quark number density, chiral condensate and the Polyakov loop at (a) $\beta = 0.75$, (b) $\beta = 0.70$, (c) $\beta = 0.65$, and (d) $\beta = 0.60$. The coefficients are determined from LQC₂D data at imaginary μ . The fitting range is $\hat{\mu}^2 = -1.15 \sim 0$ for (b) and $\hat{\mu}^2 = -(\pi/2)^2 \sim 0$ for the other cases.

function	A	B	C	$\chi^2/\text{d.o.f}$
Eq.(26)	0.66802(204)	-0.02868(167)		0.109
Eq.(26)	0.66871(257)	-0.02637(557)	0.00113(260)	0.089

TABLE IV: Coefficients of analytic functions and $\chi^2/\text{d.o.f}$ for the pseudo-critical line. The coefficients are determined from LQC₂D data at imaginary μ . The fitting range is $\hat{\mu}^2 = -(\pi/2)^2 \sim 0$ for all the cases.

-
- [1] Z. Fodor, and S. D. Katz, Phys. Lett. B **534**, 87 (2002).
- [2] C. R. Allton, S. Ejiri, S. J. Hands, O. Kaczmarek, F. Karsch, E. Laermann, Ch. Schmidt, and L. Scorzato, Phys. Rev. D **66**, 074507 (2002).
- [3] S. Ejiri et al., Phys. Rev. D **82**, 014508 (2010).
- [4] P. de Forcrand and O. Philipsen, Nucl. Phys. **B642**, 290 (2002).
- [5] M. D'Elia and M. P. Lombardo, Phys. Rev. D **67**, 014505 (2003).
- [6] L. K. Wu, X. Q. Luo, and H. S. Chen, Phys. Rev. **D76**, 034505 (2007).
- [7] M. D'Elia and F. Sanfilippo, Phys. Rev. D **80**, 111501 (2009).
- [8] P. de Forcrand and O. Philipsen, Phys. Rev. Lett. **105**, 152001 (2010).
- [9] K. Nagata and A. Nakamura, Phys. Rev. D **83**, 114507 (2011).
- [10] J. Takahashi, K. Nagata, T. Saito, A. Nakamura, T. Sasaki, H. Kouno, and M. Yahiro Phys. Rev. D **88**, 114504 (2013); J. Takahashi, H. Kouno, and M. Yahiro Phys. Rev. D **91**, 014501 (2015).
- [11] G. Aarts, Phys. Rev. Lett. **102**, 131601 (2009).
- [12] G. Aarts, L. Bongiovanni, E. Seiler, D. Sexty, and I.-O. Stamatescu, Eur. Phys. J. A **49**, 89 (2013).
- [13] D. Sexty, Phys. Lett. B **729**, 108 (2014).
- [14] M. Cristoforetti, F. Di Renzo, and L. Scorzato, Phys. Rev. D **86**, 074506 (2012).
- [15] H. Fujii, D. Honda, M. Kato, Y. Kikukawa, S. Komatsu and T. Sano, JHEP **1310**, 147 (2013).
- [16] A. Nakamura, Phys. Lett. **149B**, 391 (1984).
- [17] J. B. Kogut, D. K. Sinclair, S. J. Hands, and S. E. Morrison, Phys.Rev.D **64**, 0194505(2001).
- [18] S. Muroya, A. Nakamura and C. Nonaka, Phys. Lett. B **551**, 305 (2003).
- [19] S. Hands, P. Sitch and J.-I. Skullerud, Phys.Lett. B **662**, 405(2008).
- [20] S. Hands, S. Cotter, P. Giudice, J. Skullerud, arXiv:1210.6559.
- [21] S. Cotter, J. Skullerud, P. Giudice, S. Hands, S. Kim, and D. Mehta, PoS 091 (Lattice 2012), arXiv:1210.6757; S. Cotter, P. Giudice, S. Hands, J. Skullerud, Phys.Rev.D **87**, 034507(2013).
- [22] P. Cea, L. Cosmai, M. D'Elia and A. Papa, in two-color QCD," JHEP **0702**, 066 (2007) [hep-lat/0612018].
- [23] P. Cea, L. Cosmai, M. D'Elia and A.Papa, Phys. Rev. D **77**, 051501(R) (2008).
- [24] A. Roberge, and N. Weiss, Nucl. Phys. **B275**, 734 (1986).
- [25] K. Kashiwa, T. Sasaki, H. Kouno, M. Yahiro, Phys.Rev.D **87**, 016015(2013).
- [26] P. N. Meisinger, and M. C. Ogilvie, Phys. Lett. B **379**, 163 (1996).
- [27] A. Dumitru, and R. D. Pisarski, Phys. Rev. D **66**, 096003 (2002).
- [28] K. Fukushima, Phys. Lett. B **591**, 277 (2004).
- [29] S. K. Ghosh, T. K. Mukherjee, M. G. Mustafa, and R. Ray, Phys. Rev. D **73**, 114007 (2006).
- [30] E. Megías, E. R. Arriola, and L. L. Salcedo, Phys. Rev. D **74**, 065005 (2006).
- [31] C. Ratti, M. A. Thaler, and W. Weise, Phys. Rev. D **73**, 014019 (2006).
- [32] S. Rößner, C. Ratti, and W. Weise, Phys. Rev. D **75**, 034007 (2007).
- [33] K. Kashiwa, M. Matsuzaki, H. Kouno, Y. Sakai and M. Yahiro, Phys. Rev. D **79**, 076008 (2009).
- [34] Y. Sakai, K. Kashiwa, H. Kouno and M. Yahiro, Phys. Rev. D **77**, 051901 (2008).
- [35] H. Kouno, Y. Sakai, K. Kashiwa and M. Yahiro, J. Phys. G **36**, 115010 (2009).
- [36] Y. Sakai, K. Kashiwa, H. Kouno, M. Matsuzaki, and M. Yahiro, Phys. Rev. D **78**, 076007 (2008).
- [37] K. Kashiwa, H. Kouno, M. Matsuzaki, and M. Yahiro, Phys. Lett. B **662**, 26 (2008).
- [38] J. Sugano, J. Takahashi, M. Ishii, H. Kouno, and M. Yahiro, Phys. Rev. D **90**, 037901 (2014).
- [39] T. Sasaki, N. Yasutake, M. Kohno, H. Kouno, and M. Yahiro, arXiv:1307.0681[hep-ph] (2013).
- [40] Y. Sakai, K. Kashiwa, H. Kouno, M. Matsuzaki, and M. Yahiro, Phys. Rev. D **79**, 096001 (2009).
- [41] K. Kashiwa, T. Hell, and W. Weise, Phys. Rev. D **84**, 056010 (2011).
- [42] Y. Iwasaki, Nucl. Phys. **B258**, 141 (1985).
- [43] S. Itoh, Y. Iwasaki and T. Yoshié, Phys. Letts **147B**, 141 (1984).
- [44] B. Sheikholeslami and R. Wohlert, Nucl. Phys. **B259**, 572 (1985).
- [45] G. P. Lepage and P. B. Mackenzie, Phys. Rev. D **48**, 2250 (1993).
- [46] Y. Iwasaki, UTHEP-118 (1983) arXiv: 1111.7054.
- [47] W.Pauli, Nuovo Cimento **6**, 205 (1957).
- [48] W.Pauli,ibid **7**, 411.
- [49] T.Brauner, K. Fukushima, and Y. Hidaka, Phys. Rev. D **80**, 074035(2009).
- [50] Y. Sakai, T. Sasaki, H. Kouno, and M. Yahiro, Phys. Rev. D **82**, 076003 (2010).
- [51] Y. Aoki, G. Endrödi, Z. Fodor, S. D. Katz and K. K. Szabó, Nature **443**, 675 (2006).
- [52] M. P. Lombardo, Pos **LAT2005**(2006) 168, hep-lat/0509181 (2005).